The Spitzer Survey of Stellar Structure in Galaxies (S4G)
Author(s): Kartik Sheth, Michael Regan, Joannah L. Hinz, Armando Gil de Paz, Karín Menéndez-Delmestre, Juan-Carlos Muñoz-Mateos, Mark Seibert, Taehyun Kim, Eija Laurikainen, Heikki Salo, Dimitri A. Gadotti, Jarkko Laine, Trisha Mizusawa, Lee Armus, E. Athanassoula, Albert Bosma, Ronald J. Buta, Peter Capak, Thomas H. Jarrett, Debra M. Elmegreen, Bruce G. Elmegreen, Johan H. Knapen, Jin Koda, George Helou, Luis C. Ho, Barry F. Madore ...
Source: *Publications of the Astronomical Society of the Pacific*, Vol. 122, No. 898 (December 2010), pp. 1397-1414
Published by: The University of Chicago Press on behalf of the Astronomical Society of the Pacific
Stable URL: http://www.jstor.org/stable/10.1086/657638
Accessed: 24/01/2011 11:10

PUBLICATIONS OF THE ASTRONOMICAL SOCIETY OF THE PACIFIC, **122**:1397–1414, 2010 December

The *Spitzer* Survey of Stellar Structure in Galaxies (S^{4}G)

KARTIK SHETH,[1,2,3] MICHAEL REGAN,[4] JOANNAH L. HINZ,[5] ARMANDO GIL DE PAZ,[6] KARÍN MENÉNDEZ-DELMESTRE,[7]
JUAN-CARLOS MUÑOZ-MATEOS,[6] MARK SEIBERT,[7] TAEHYUN KIM,[1,8] EIJA LAURIKAINEN,[9,10] HEIKKI SALO,[9]
DIMITRI A. GADOTTI,[11,12] JARKKO LAINE,[9,10] TRISHA MIZUSAWA,[2,3] LEE ARMUS,[2,3] E. ATHANASSOULA,[13]
ALBERT BOSMA,[13] RONALD J. BUTA,[14] PETER CAPAK,[2,3] THOMAS H. JARRETT,[2,3]
DEBRA M. ELMEGREEN,[15] BRUCE G. ELMEGREEN,[16] JOHAN H. KNAPEN,[17,18]
JIN KODA,[18] GEORGE HELOU,[2,3] LUIS C. HO,[7] BARRY F. MADORE,[7]
KAREN L. MASTERS,[19] BAHRAM MOBASHER,[20] PATRICK OGLE,[2,3]
CHIEN Y. PENG,[21] EVA SCHINNERER,[22] JASON A. SURACE,[2,3]
DENNIS ZARITSKY,[5] SÉBASTIEN COMERÓN,[16]
BONITA DE SWARDT,[23] SHARON E. MEIDT,[22]
MANSI KASLIWAL,[3] AND MANUEL ARAVENA[1]

Received 2010 April 22; accepted 2010 October 6; published 2010 December 2

ABSTRACT. The *Spitzer* Survey of Stellar Structure in Galaxies (S^{4}G) is an Exploration Science Legacy Program approved for the *Spitzer* post–cryogenic mission. It is a volume-, magnitude-, and size-limited ($d < 40$ Mpc, $|b| > 30°$, $m_{B\mathrm{corr}} < 15.5$, and $D_{25} > 1'$) survey of 2331 galaxies using the Infrared Array Camera (IRAC) at 3.6 and 4.5 μm. Each galaxy is observed for 240 s and mapped to $\geq 1.5 \times D_{25}$. The final mosaicked images have a typical 1σ rms noise level of 0.0072 and 0.0093 MJy sr^{-1} at 3.6 and 4.5 μm, respectively. Our azimuthally averaged surface brightness profile typically traces isophotes at $\mu_{3.6\mu\mathrm{m}}(\mathrm{AB})(1\sigma) \sim 27$ mag arcsec^{-2}, equivalent to a stellar mass surface density of $\sim 1\ M_{\odot}\mathrm{pc}^{-2}$. S^{4}G thus provides an unprecedented data set for the study of the distribution of mass and stellar structures in the local universe. This large, unbiased, and extremely deep sample of all Hubble types from dwarfs to spirals to ellipticals will allow for detailed structural studies, not only as a function of stellar mass, but also as a function of the local environment. The data from this survey will serve as a vital testbed for cosmological simulations predicting the stellar mass properties of present-day galaxies. This article introduces the survey and describes the sample selection, the significance of the 3.6 and 4.5 μm bands for this study, and the data collection and survey strategies. We describe the S^{4}G data analysis pipeline and present measurements for a first set of galaxies, observed in both the cryogenic and warm mission phases of *Spitzer*. For every galaxy we tabulate the galaxy diameter, position angle, axial ratio, inclination at $\mu_{3.6\mu\mathrm{m}}(\mathrm{AB}) = 25.5$, and 26.5 mag arcsec^{-2} (equivalent to $\approx \mu_{\mathrm{B}}(\mathrm{AB}) = 27.2$ and 28.2 mag arcsec^{-2}, respectively). These measurements will form the initial S^{4}G catalog of galaxy properties. We also measure the total magnitude and the azimuthally averaged radial profiles of ellipticity, position angle, surface brightness, and color. Finally, using the galaxy-fitting code GALFIT, we deconstruct each galaxy into its main constituent stellar components: the bulge/spheroid, disk, bar, and nuclear point source, where necessary. Together, these data products will provide a comprehensive and definitive catalog of stellar structures, mass, and properties of galaxies in the nearby universe and will enable a variety of scientific investigations, some of which are highlighted in this introductory S^{4}G survey paper.

Online material: color figures, extended table

[1] National Radio Astronomy Observatory (NAASC), 520 Edgemont Road, Charlottesville, VA 22903.
[2] Spitzer Science Center.
[3] California Institute of Technology, 1200 East California Boulevard, Pasadena, CA 91125.
[4] Space Telescope Science Institute, 3700 San Martin Drive, Baltimore, MD 21218.
[5] University of Arizona, 933 North Cherry Ave, Tucson, AZ 85721.
[6] Departamento de Astrofsica, Universidad Complutense de Madrid, Madrid 28040, Spain.
[7] The Observatories, Carnegie Institution of Washington, 813 Santa Barbara Street, Pasadena, CA 91101.
[8] Astronomy Program, Department of Physics and Astronomy, Seoul National University, Seoul 151-742, Korea.
[9] Department of Physical Sciences/Astronomy Division, University of Oulu, FIN-90014, Finland.
[10] Finnish Centre for Astronomy with ESO (FINCA), University of Turku.
[11] Max-Planck-Institut für Astrophysik, Karl-Schwarzschild-Strasse 1, D-85748 Garching bei Munchen, Germany.

1. INTRODUCTION

Understanding the distribution of stars within a galaxy is akin to the study of the endoskeleton of a body; embedded within the galaxy is the fossil record of the assembly history and evolutionary processes of cosmic time. The first step in unraveling this history is to obtain a complete census of the stellar structures in galaxies in the local volume. This is the primary motivation for the *Spitzer* Survey of Stellar Structures in Galaxies (S^{4}G). S^{4}G is a volume-limited ($d < 40$ Mpc), size-limited ($D_{25} > 1'$), and apparent B-band brightness-limited (corrected for inclination, Galactic extinction, and K-correction) ($m_{B\mathrm{corr}} < 15.5$) survey of 2331 nearby galaxies at 3.6 and 4.5 μm with the Infrared Array Camera (IRAC) (Fazio et al. 2004) at the Spitzer Science Center (Werner et al. 2004).

Over the last 70 years, numerous surveys have sought to create baseline data sets for nearby galaxies with as few as tens of galaxies (ACS Nearby Galaxy Survey Treasury [ANGST], Dalcanton et al. 2009; Spitzer Infrared Nearby Galaxies Survey [SINGS], Kennicutt et al. 2003) to tens of thousands of galaxies (e.g., Third Reference Catalogue of Bright Galaxies [RC3], de Vaucouleurs et al. 1991). While these surveys were designed specifically for particular scientific goals, none of them provides an accurate inventory of the stellar mass and the stellar structures in nearby galaxies. The main reason is that infrared surveys, where light from the old stellar population is better measured due to reduced dust extinction and contamination from star formation, are extremely difficult to conduct from the ground. The largest ground-based infrared surveys (e.g., Two Micron All Sky Survey [2MASS], Skrutskie et al. 2006; Deep Near Infrared Survey of the Southern Sky [DENIS], Epchtein et al. 1994; Paturel et al. 2003b) are rather shallow in depth, and as a result, studies of nearby galaxies have been restricted to high surface brightness inner disks. In contrast, deeper infrared surveys (e.g., Ohio State University Bright Galaxy Survey [OSUBGS], Eskridge et al. 2002, Near-Infrared SO Survey [NIRSOS], Laurikainen et al. 2010) have imaged only a few hundred galaxies. S^{4}G is specifically designed to provide over an order-of-magnitude improvement in the sample size and several-magnitudes-deeper data than existing surveys.

S^{4}G builds upon the two previous *Spitzer* Legacy surveys of nearby galaxies: SINGS (Kennicutt et al. 2003) and the Local Volume Legacy (LVL) survey (Lee et al. 2008). SINGS was designed to probe star formation, dust, and polycyclic aromatic hydrocarbon (PAH) emission in all representative environments *within* galaxies in a sample of 75 objects. The LVL survey was designed to study spatially resolved star formation and the red stellar population within galaxies in a local volume of 11 Mpc. The local volume limits the 258 LVL galaxies to consist mostly of dwarf, irregular, and late-type systems (see the histogram in Fig. 1). The remainder of the *Spitzer* archive from the cryogenic mission is inadequate for the science goals outlined here, because it lacks sufficient numbers of galaxies of all stellar masses, particularly at $M_* < 109\ M_\odot$, Hubble types, and environments. As shown in Figures 1 and 2, S^{4}G explores the full range of stellar structures in a representative and large sample of galaxies of all types and masses and in diverse environments. S^{4}G is designed to provide the ultimate baseline data set for the study of stellar structures and mass in nearby galaxies.

In this article we introduce S^{4}G, describe the data collection and analysis strategy, and briefly describe the variety of scientific investigations possible with these data. All S^{4}G galaxies are processed through a uniform pipeline to create the deepest and largest mid-infrared image catalog of nearby galaxies to date. For every galaxy we measure the magnitude and surface brightness and tabulate the galaxy diameter, position angle, axial ratio, and inclination at $\mu_{3.6\mu\mathrm{m}}(\mathrm{AB}) = 25.5$ and 26.5 mag arcsec^{-2}. We also compute the azimuthally averaged radial profiles of ellipticity, position angle, surface brightness, and color. This fundamental catalog of galaxy properties will allow us to classify their morphology based on their stellar structures—a preliminary study is presented in Buta et al. (2010). In the long term, the main goal of the S^{4}G project is to obtain a detailed understanding of the properties of the different stellar structures, their formation and evolutionary paths, and their role in the broader picture of galaxy evolution. This will be done by decomposing every galaxy into its constituent structural components (e.g., bulge/spheroid, bar, disk, and nuclear point source) using GALFIT (Peng et al. 2002, 2010).

A number of scientific studies are already underway by the S^{4}G team. These include a study of outer disks to determine the variety and frequency of different disk profile(s), truncations or thresholds and their relationship to the buildup of galaxy disks, a study of shells and debris around galaxies and their

[12] European Southern Observatory, Casilla 19001, Santiago 19, Chile.
[13] Laboratoire d'Astrophysique de Marseille (LAM), UMR6110, Université de Provence/CNRS, Technopôle de Marseille Etoile, 38 rue Frédéric Joliot Curie, 13388 Marseille Cédex 20, France.
[14] Department of Physics and Astronomy, University of Alabama, Box 870324, Tuscaloosa, AL 35487.
[15] Vassar College, Dept. of Physics and Astronomy, Poughkeepsie, NY 12604.
[16] IBM Research Division, T. J. Watson Research Center, Yorktown Hts., NY 10598.
[17] Instituto de Astrofsica de Canarias, E-38200 La Laguna, Spain.
[18] Departamento de Astrofísica, Universidad de La Laguna, Spain.
[19] Institute of Cosmology and Gravitation, University of Portsmouth, Dennis Sciama Building, Burnaby Road, Portsmouth, PO1 2EH, UK.
[20] Department of Physics and Astronomy, University of California, Riverside, CA 92521
[21] NRC Herzberg Institute of Astrophysics, 5071 West Saanich Road, Victoria, V9E 2E7, Canada.
[22] Max-Planck-Institut für Astronomie, Königstuhl 17, 69117 Heidelberg, Germany.
[23] South African Astronomical Observatory, Observatory, 7935 Cape Town, South Africa.

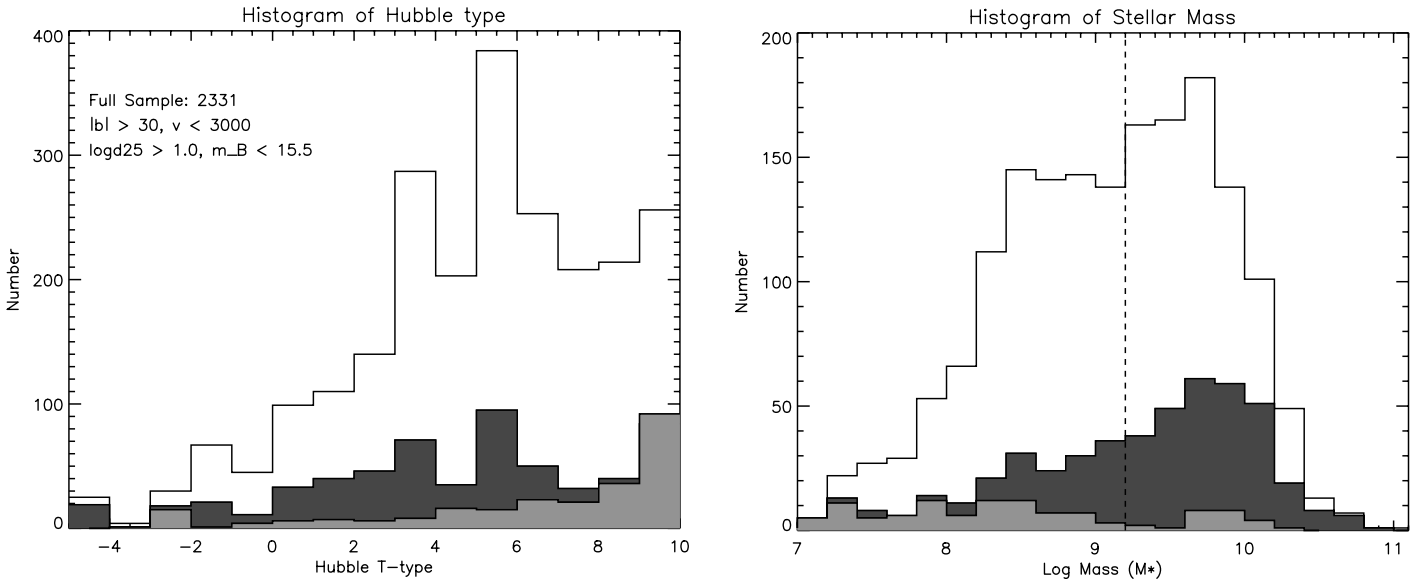

FIG. 1.—*Left:* Histogram of all galaxies in S^{4}G as a function of the Hubble T-type. The filled histograms show archival data from the LVL (*light gray*) and other GO/GTO (*dark gray*) data. *Right:* Histogram of masses for the S^{4}G sample galaxies, where masses are calculated from the 2MASS photometry assuming the M/L function from Bell et al. (2003). The biggest gains in building a statistically complete sample are for galaxies with $\log(M/M_{\odot}) < 9.2$. See the electronic edition of the *PASP* for a color version of this figure.

relationship to central star formation or active galactic nucleus (AGN) activity, an analysis of the structural properties of bulges/spheroids (classical, disky, and boxy/peanut-shaped), determination of the bar fraction and bar properties in relationship to the host galaxies and environment, an analysis of the stellar arm-interarm variations in spirals, an investigation of the

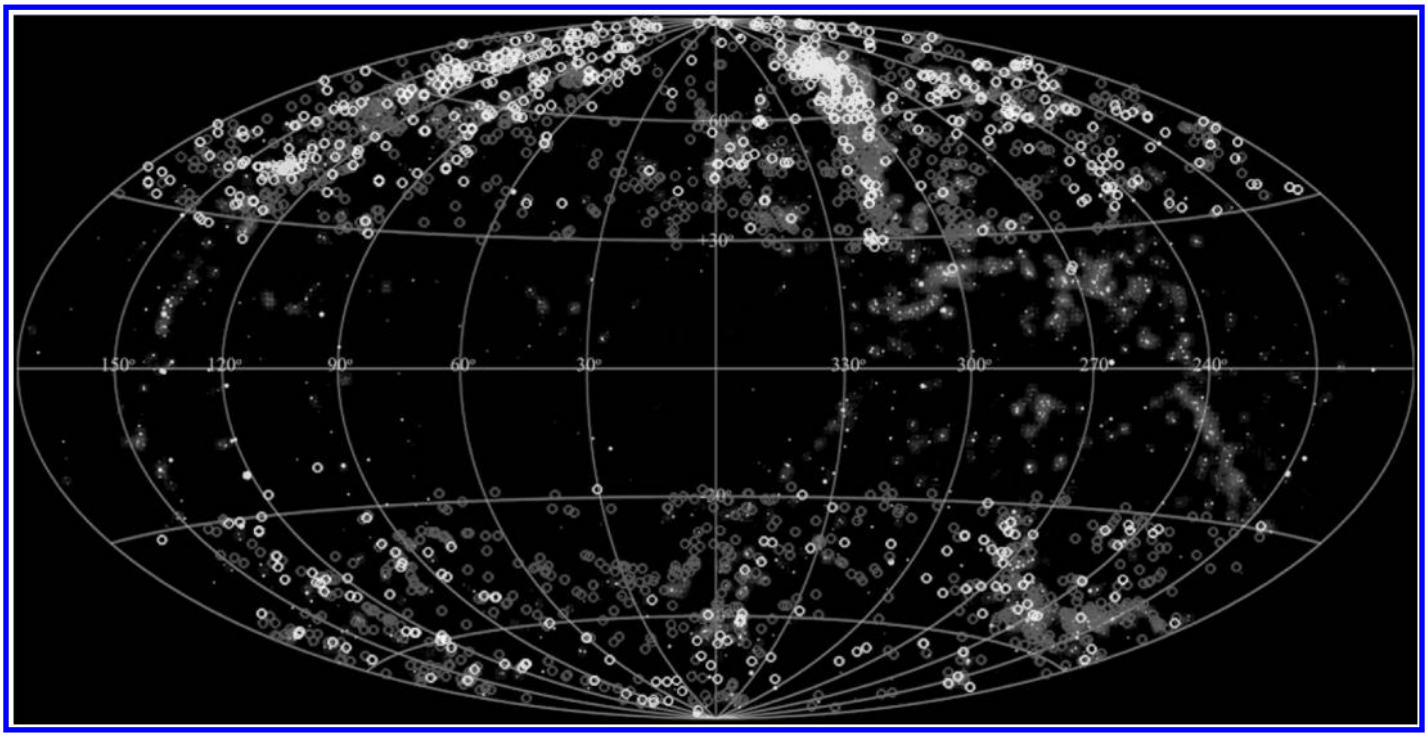

FIG. 2.—Galaxies from S^{4}G plotted on the local large-scale structure map from the 2MASS XSC (Jarrett 2004). The white circles show the warm mission S^{4}G galaxies to be observed. The gray circles show LVL and GO/GTO archival galaxies. With the full S^{4}G sample, we will have the ability to make a less biased study of the galaxy host properties as a function of the local large-scale structures. See the electronic edition of the *PASP* for a color version of this figure.

underlying old stellar population in rings and a search for fossil rings, an analysis of the old stellar content of dwarf galaxies and its implication for their formation history, etc. Longer-term studies include star formation history and assembly of galaxies using *GALEX* and Hα data, the Tully—Fisher relationship using existing H I data (e.g., Arecibo Legacy Fast ALFA [ALFALFA] survey, Giovanelli et al. 2005; H I Parkes All Sky Survey [HIPASS], Barnes et al. 2001), and testing of new mid-infrared diagnostics of AGN. We describe these studies in more detail in § 6. Ultimately, S^{4}G will lead to numerous other studies of astrophysical phenomena in the nearby universe and will provide a key anchoring data set for studies of galaxy evolution.

2. THE *Spitzer* 3.6 AND 4.5 μm BANDS: BEST TRACERS OF STELLAR MASS

The 3.6 and 4.5 μm IRAC bands on *Spitzer* are ideal tracers of the stellar mass distribution in galaxies, because they image the Rayleigh-Jeans limit of the blackbody emission for stars with $T > 2000$ K. Moreover, the mid-infrared (3.6–4.5) color in nearby galaxies is nearly constant with radius and is independent of the age of the stellar population and its mass function (Pahre et al. 2004). Analysis of the tilt in the fundamental plane for ellipticals shows that the *Spitzer* IRAC bands are better tracers of the stellar mass than even K-band emission, which is more sensitive to variations in the underlying stellar population; the IRAC data are more uniform and are therefore the best, and perhaps most direct, tracers of stellar mass (Jun & Im 2008). Additionally, on *Spitzer* these bands are so sensitive that S^{4}G will image to extremely low stellar mass surface densities ($\sim$1 $M_\odot$ pc^{-2}).

There are minor contaminants to the old stellar population light in the 3.6 and 4.5 μm IRAC bands. In the 3.6 μm band, there is a very weak 3.3 μm PAH feature, which contributes negligibly to the overall emission in the band (less than 2%, as the equivalent width is $\sim$0.02 μm; Tokunaga et al. 1991). Hot dust ($Td > 500$ K) from very small grains can contribute light to both bands, with a higher contribution in the 4.5 μm band, but this condition occurs only near active galactic nuclei or extreme starbursts. By examining the colors of the galaxies, we should be able to use the two IRAC bands to remove the effects of the 3.3 μm PAH or hot dust emission. Another important advantage of having two bands is that by co-adding them, we can further improve the signal-to-noise ratio (S/N) and push the study to even fainter regions of the galaxies. In both bands, the contamination from young red supergiants is also very low. From previous studies, it is known that in the near-infrared, the overall contamination from young red supergiants to a galaxy is only $\sim$3%, but in regions of star formation, the contribution may be as high as 25% (Rhoads 1998). These regions are easily identifiable, however, and can be flagged. At the IRAC wavelengths, the fractional contribution from star-forming regions is expected to be the same (or lower), because these wavebands are at longer wavelengths on the Rayleigh-Jeans tail of the spectral energy distribution. At these wavelengths, there is lower dust extinction (Draine & Lee 1984) and no other significant emission sources. Thus, with the extremely low surface brightness limits, S^{4}G offers a unique and virtually dust-free view of the distribution of mass in stellar structure in the nearby universe.

Although ground-based near-infrared observations can offer higher angular resolution than *Spitzer*, the main obstacle for ground-based observations is the very high and variable sky brightness (typically $\mu_K \sim 13.4$ mag arcsec^{-2}). The surface brightness level in the IRAC data is over 10 mag below the typical sky brightness level. To get to this level from the ground, one would need to characterize the sky brightness, flat field, and instrumental variations to better than 0.0009%. This is currently not possible with any existing (or planned) near-infrared survey. Surveys like UKIDSS LAS (UKIRT Infrared Deep Sky Survey Large Area Survey) or VISTA VHS (Visible and Infrared Survey Telescope for Astronomy VISTA Hemisphere Survey) are planning to reach a depth of 18.4 (21.2 in AB) mag arcsec^{-2} in the K_s band, which translates to 30 $L_\odot$ pc^{-2} (even with the brighter stellar emission at K_s band), whereas S^{4}G reaches $\sim$2 $L_\odot$ pc^{-2}. It is the stability of the background that is the biggest advantage for space-based observations.

3. SAMPLE SELECTION

We chose all galaxies with radial velocity $V_{\rm radio} < 3000$ km/s (corresponding to a distance $d < 40$ Mpc for a Hubble constant of 75 km/s/Mpc), total corrected blue magnitude $m_{B\rm corr} < 15.5$, blue light isophotal angular diameter $D_{25} > 1.0'$ at Galactic latitude $|b| > 30°$ using HyperLEDA (Paturel et al. 2003a). The choice of $V_{\rm radio}$ does limit the sample to galaxies with radio-derived (e.g., H I) radial velocities in HyperLEDA and, as a result, misses some galaxies for which only optically derived radial velocities exist; currently, a sample chosen with $V_{\rm optical}$ instead of $V_{\rm radio}$ would contain 2997 galaxies. A comparison of the galaxy properties of the two samples shows that the S^{4}G sample misses galaxies that are small, relatively faint, and early-type (gas-poor) systems from the volume surveyed.

We also note that our sample was defined using HyperLEDA in September 2007—since then, 98 more galaxies have been added to the HyperLEDA database that meet the S^{4}G criteria described previously, and we expect that some more may be added as better data become available. Given the limited lifetime of *Spitzer*, we are unable to go back and acquire data on these additional galaxies, but we expect that the few percent of additional galaxies will not strongly influence the core characteristics of the sample, except for the bias against early-type galaxies as noted previously.

The choice of a 40 Mpc volume is arbitrary—it was chosen to be large enough to provide a statistically significant number of galaxies of all types and to be representative of a large range of the local large-scale structure environment (as shown in Fig. 2). Our experience with previous surveys of galaxy

properties (e.g., Sheth et al. 2008) has shown that a few thousand galaxies are needed to accurately measure and account for completeness effects in mass, color, and size selection of galaxy samples for robust investigations of relationships between galactic structure and host galaxy properties. The size cut, $\log D_{25} > 1.0$, was made to ensure that galaxies were large enough for a detailed study of their internal structure (at 40 Mpc, $1' \sim 11.6$ kpc). The apparent size and apparent magnitude cut were chosen to match the RC3 limits. The Galactic latitude cut, $|b| > 30°$, was used to minimize the unresolved Galactic light contribution from the Milky Way disk. The full sample of 2331 S^{4}G galaxies is listed in Table 1. In Figure 1, we show the distribution of S^{4}G galaxies as a function of Hubble type and stellar mass, along with the existing distribution of the LVL galaxies (*green*) and guest observer (GO) and guaranteed-time observer (GTO) galaxies (*blue*), including the SINGS galaxies. There are some noteworthy subsamples within S^{4}G. There are 188 early-type galaxies (ellipticals and lenticulars), 206 dwarf galaxies (defined as $M_B > -17$), of which 135 are DDO dwarfs, and 465 edge-on ($i > 75°$) systems. Over 800 of the S^{4}G galaxies are mapped beyond a diameter of $3 \times D_{25}$. These subsamples provide the deepest, largest, and most homogeneous samples for a multitude of galaxy evolutionary studies, some of which are described in § 6.

3.1. Archival/Cryogenic *Spitzer* Data

Of the 2331 galaxies in the S^{4}G sample, 597 had some existing data at 3.6 and 4.5 μm from the *Spitzer* cryogenic mission; 125 of these are part of the LVL survey, and 56 are from the SINGS survey, both of which used the same observing strategy (§ 4) that we employ for S^{4}G. Almost all of the archival maps have at least 240 s of integration time per pixel and are sufficiently deep. The only exceptions are NGC 5457 (96 s); NGC 0470 and NGC 0474 (150 s); and NGC 5218, NGC 5216, and NGC 5576 (192 s).

In terms of area, 82 of the archival galaxies were mapped between 1.0 and $1.5 \times D_{25}$, and 43 others were mapped to less than $1.0 \times D_{25}$. While outer disk science for these 125 galaxies would benefit from an extended map, they represent only a small fraction of the total sample, and the repetition of observations would have yielded only an incremental scientific return. Therefore, we decided not to repeat observations of any of the archival galaxies. We also decided not to map the SMC and the LMC, which meet our selection criteria but are very large and are being observed as part of other GO programs. M33, the other commonly studied Local Group galaxy, was observed during the cryogenic mission and is included in the archival part of our sample. All other galaxies that were found via the HyperLEDA database search in 2007 September are observed (see the earlier note about the modest additions to the HyperLEDA database in the last three years). Although we do not repeat observations of any of the archival galaxies, we are processing all galaxies in the S^{4}G sample, except the SMC and LMC, through the same S^{4}G reduction and analysis pipelines described in § 5.

4. *Spitzer* POST–CRYOGENIC MISSION OBSERVATION STRATEGY

The 1734 S^{4}G galaxies being observed in the post–cryogenic mission are mapped using either a small dithered map or a mosaicked observation with both IRAC channels' on-source integration time of 240 s, which leads to an rms noise of $\mu(1\sigma) \sim 0.0072$ and 0.0093 MJy sr^{-1} at 3.6 and 4.5 μm, respectively. This translates to a typical surface brightness sensitivity

TABLE 1

RC3-LIKE PARAMETERS FOR GALAXIES

Galaxy	R.A. (J2000)	Decl. (J2000)	T	M_B	Log(D_{25})	$m_{B\mathrm{corr}}$
UGC12893	0.00784	17.21952	8.4	−15.97	1.06	15.14
PGC000143	0.03292	−15.4614	9.9	−15.83	2.04	10
ESO012−014	0.04511	−80.34825	9	−18.17	1.18	13.72
NGC7814	0.05418	16.14554	2	−20.04	1.64	10.96
UGC00017	0.06198	15.21822	9	−16.02	1.39	14.6
NGC7817	0.06635	20.75182	4.1	−21.11	1.52	11.56
ESO409-015	0.09223	−28.09915	6.2	−15.16	1.02	14.43
ESO293-034	0.10559	−41.49592	6	−18.68	1.4	12.67
NGC0007	0.13916	−29.91678	4.9	−18.22	1.39	13.18
NGC0014	0.14618	15.81659	9.8	−18.25	1.18	12.35
IC1532	0.16464	−64.37161	4	−17.89	1.26	13.86

NOTE.—All properties obtained from the HyperLEDA database (http://leda.univ-lyon1.fr/). R.A. and Decl. are decimal hours and degrees in J2000; T is the morphological type code (-5 : E, -3 : E − S0, 0 : S0a, 3 : Sb, 7 : Sd, and 10 : Irr); M_B is the absolute B magnitude; and Log (D_{25}) is the apparent major axis diameter at 25 mag arcsec^{-2}; . D_{25} is in units of $0.1'$; and $m_{B\mathrm{corr}}$ is the total apparent corrected B magnitude, corrected for inclination, Galactic extinction, and K-correction. A value of -99 indicates that the value was missing from the HyperLEDA database. Table 1 is published in its entirety in the electronic edition of the *PASP*. A portion is shown here for guidance regarding its form and content.

of $\mu_{AB} \sim 27$ mag arcsec^{-2} or a stellar surface density of 1.13 $M_{\odot}$ pc^{-2}, assuming a solar $M_K = 3.33$ (Worthey 1994) and $M/L_K = 1$ (Heraudeau & Simien 1997).

Of the new observations, 1560 are of galaxies with $D_{25} < 3.3'$. We can map these galaxies to $1.5 \times D_{25}$ with a single pointing, because the *Spitzer* field of view is 5′. Hence, all of these galaxies are mapped using a standard-cycling small dither pattern with four exposures of 30 s each in two separate Astronomical Observation Requests (AORs). Each pair of AORs is separated by at least 30 days to allow for sufficient rotation of the telescope so that the galaxy is imaged at two distinct orientations. Two AORs allow us to better remove cosmic rays, and the redundant information gathered by the two visits allows us to characterize and remove image artifacts (e.g., muxbleed, column pulldown, etc.; see Carey et al. 2010) and possible asteroids. Drizzling the data from the two visits also allows us to achieve subpixel sampling with which we can reconstruct images with better fidelity than would be possible from a single visit. We also note that since both the 3.6 and 4.5 μm arrays collect data simultaneously, their offset placement in the *Spitzer* focal plane means that an additional flanking map is made adjacent to the galaxy in each of the two channels (in some cases, the flanking field from each of the AORs may not overlap exactly, due to the telescope rotation, but this does not affect the observations of the main galaxy). An example of a typical dithering AOR is shown in the left panel in Figure 3.

One of the considerations in designing these AORs was the effect of saturation from bright stars on the chip and the scattered light from bright stars falling in one of the three scattering zones surrounding the arrays.[24] Stars brighter than fifth magnitude can leave a latent charge on the chip. Stars brighter than 11th magnitude in the scattering zones may scatter light into the main field of view of the IRAC chips. To mitigate these cases, we used the *Spitzer* Observing Tool (SPOT[25]) to examine every galaxy with a star, $m_{Ks} < 8$ (stars fainter than $m_{Ks} = 8$ do not contribute significantly to the background) within an area of 300″, covering the IRAC field of view and scattering zones adequately, for all possible visibility windows through 2011. In a majority of these cases, no modifications of AORs were needed, because the offending star(s) fell out of the chip or the scattering zones. In the remaining cases, we constructed AORs with timing constraints, slightly offset pointings, or used medium dithers or mosaics to reduce the effect of the bright stars.

For galaxies with $D_{25} > 3.3'$, we mosaic them in array coordinates with offsets of 146.6″ with 30 s integrations at each location to create a map $\geq 1.5 \times D_{25}$. This leads to a map with each pixel observed four times at all wavelengths in the core of the map. In addition, on each side of the galaxy there will be a region where each pixel is observed twice, but only in one of the two channels. Like the dithered AORs, each mosaic is observed twice, but with only a follow-on constraint so that each mosaic overlaps the other closely. An example of this type of an AOR is shown in the right panel of Figure 3.

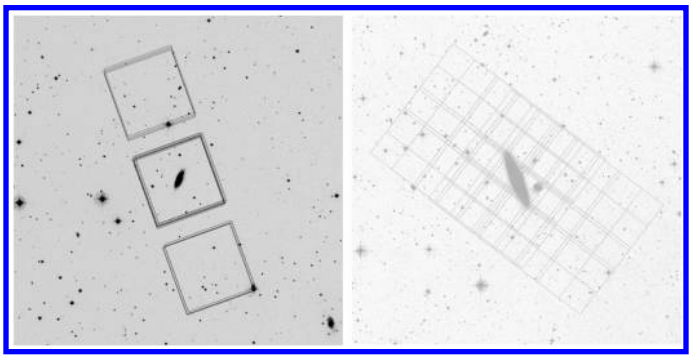

FIG. 3.—*Left:* A typical dithering AOR shown for NGC 2919 in the warm mission. The overlay shows the 3.6 μm (4.5 μm) coverage. The galaxy is mapped in two separate AORs separated by at least 30 days. The flanking fields are reduced by the S^{4}G pipeline and may also contain serendipitous objects such as interacting galaxies or tidal debris. *Right:* A typical mosaicking AOR shown for NGC 1515 in the warm mission. The grids show the coverage of the 3.6 μm and 4.5 μm cameras. The galaxy is mapped to $>1.5 \times D_{25}$ by both arrays. The mosaicking pattern takes steps of 146.6″ with 30 s integrations in each location. The total 240 s integration time is obtained in two separate AORs. Note that significant amounts of sky are also mapped on opposite ends of the galaxy by each of the individual arrays. See the electronic edition of the *PASP* for a color version of this figure.

Although larger mosaics could be made, our experience with SINGS data showed that the dominant noise term comes from variations of the background (Regan & Teuben 2004; Regan et al. 2006). The best background for a galaxy includes sufficient sky not far from the area of interest. Our map sizes are thus fine-tuned to achieve the best possible S/N for all galaxies.

5. THE S^{4}G PIPELINE

The S^{4}G pipeline is divided into four distinct parts, which we refer to as Pipelines 1, 2, 3, and 4. Pipeline 1 takes the raw basic calibrated data FITS (Flexible Image Transport System) files and converts them to science-ready data. Pipeline 2 creates a mask for the foreground and background objects for each of the individual galaxies. Pipeline 3 measures the standard global galaxy properties such as size, axial ratio, magnitude, color, etc., and computes the radial profiles of the standard properties. Pipeline 4 deconstructs each galaxy into its major structural components. Each of these is described in detail here.

5.1. S^{4}G Pipeline 1

The purpose of Pipeline 1 (P1) is to create science-ready mosaics from the two visits of each target. To do this, P1 performs two major steps. First, it matches the background level in the individual images to account for drifts in the zero point of

[24] A description of this problem is given by Carey et al. (2010).
[25] See http://ssc.spitzer.caltech.edu/warmmission/propkit/spot/.

the amplifiers. Second, it creates the final mosaic using the Drizzle package of IRAF.[26]

To match the background levels in the individual images we find the regions of overlap between all pairs of overlapping images. Typically, we require that the overlap region contain 20,000 pixels. For all of the new post–cryogenic mission observations (and archival observations that used the same observing strategies), such an overlap is always available. However, when reducing other archival data with less overlap between the frames, we reduce the number of pixels in the overlap region to as low as 5000 pixels—this still provides an adequate number of pixels for estimating the background.

Within these regions we determine the brightness level of the 20th percentile pixel. We use the 20th percentile brightness level to better avoid detector artifacts such as muxbleed, which can affect even the median. By using the 20th percentile brightness level we have a better chance of using the true sky level. We then perform a least-squares solution using the brightness differences between all the pairs of overlapping images, minimizing the residual background difference. Since we use the difference, we need to use the background level in the first image to set the zero point of the solution. We then make corrected images by adding the solved-for corrections and use these images in the formation of the final mosaic. We create the final mosaic following the standard prescription of the Space Telescope Science Data Analysis System (STSDAS) dither package. This method removes the cosmic rays by first forming a mosaic from a median combination of the images and then comparing the individual images with the median mosaic and flagging any cosmic rays. The final mosaic is formed by drizzling the individual images. The resulting mosaic has a pixel scale of $0.75''$, and we correct for the change in pixel size to keep the units of MJy sr^{-1}.

The relative astrometry of the mosaicked images is excellent, because the *Spitzer* pipeline already incorporates the 2MASS positions to update its astrometry for each of the basic calibrated data frames. The S^{4}G pipeline therefore does not require the type of cross-correlation that was needed previously for the SINGS pipeline to align overlapping fields. The relative astrometric accuracy is less than $0.1''$.

The point-spread function (PSF) for IRAC is asymmetric and depends on the spacecraft orientation angle. Pipeline 1 images are produced by combining two different visits to the galaxy, and we therefore estimate the PSF by combining stars in the foreground and background for six typical S^{4}G galaxies to create a "super"-PSF, which has a typical FWHM of $1.7''$ and $1.6''$ at 3.6 μm and 4.5 μm, respectively. For the most distant galaxies in our survey, at a distance of $\sim$40 Mpc, this resolution corresponds to a linear scale of $\sim$300 pc. At the median distance of the galaxies in this survey of 21.6 Mpc, this corresponds to a linear scale of $\sim$170 pc.

5.2. S^{4}G Pipeline 2

After the science-ready images are produced by the S^{4}G pipeline, we generate masks for point sources using SExtractor (Bertin & Arnouts 1996) for both channels. Each mask is checked by eye and iterated to identify any point source otherwise missed by SExtractor. We also unmask any region of the galaxy that may be have been incorrectly identified by SExtractor. The images with their corresponding masks are then run through the third part of the S^{4}G pipeline (Pipeline 3, P3 hereafter).

5.3. S^{4}G Pipeline 3

The first step in P3 is to determine the local sky level around each galaxy. We want to be sufficiently far from the galaxy to ensure that there is no contamination from the galaxy, but not so far that the background is not truly local. We do this by computing the median sky value in two concentric elliptical annuli centered at the position of the galaxy. Typically, we start the inner annulus at a distance of $1.5 \times D_{25}$. This annulus is divided in azimuth into 45 regions (or sky boxes). Each of these regions is then grown outward until it encompasses a total of 4000 nonmasked pixels,[27] as shown in Figure 4. The second annulus begins at the end of the first annulus and the same process is repeated. We compare the measured sky values in the two annuli for any radial gradients that might be indicative of light contamination from the galaxy. If we find that there is contamination, then we move the inner radius outward and repeat the process until we ensure that we are sampling the local sky.

In our analysis so far, the inner radius of the inner annulus has varied between 1.2 and $2 \times D_{25}$. In all cases for the warm mission data and a majority of the archival data, it has been sufficient to set the inner radius of the annulus to either 1.5 or $2 \times D_{25}$. However, in a few cases where the archival data are shallow and the galaxy is relatively blue, we moved the inner radius to $1.2 \times D_{25}$ to be immediately outside the galaxy to get as accurate a measurement possible for the local sky level. Automating this procedure is nontrivial, because variations at these faint levels ($\mu_{3.6\mu\mathrm{m}} > 27(\mathrm{AB})$ mag arcsec^{-2}) can be from a lopsided galaxy, debris or tidal structures, or variation in the background. Therefore, we examine every galaxy by eye to ensure that contamination from the galaxy light to the measurement of the sky background is as low as possible and move the radii outward as needed.

The sky background computation method for three of the galaxies in the S^{4}G sample (NGC 0337, NGC 4450, and NGC 4579) is shown in Figure 4. In the central column of this

[26] IRAF is distributed by the National Optical Astronomy Observatories, which are operated by the Association of Universities for Research in Astronomy, Inc., under cooperative agreement with the National Science Foundation.

[27] For archival galaxies that fill the mosaicked frame, this requirement is reduced to 1000 nonmasked pixels.

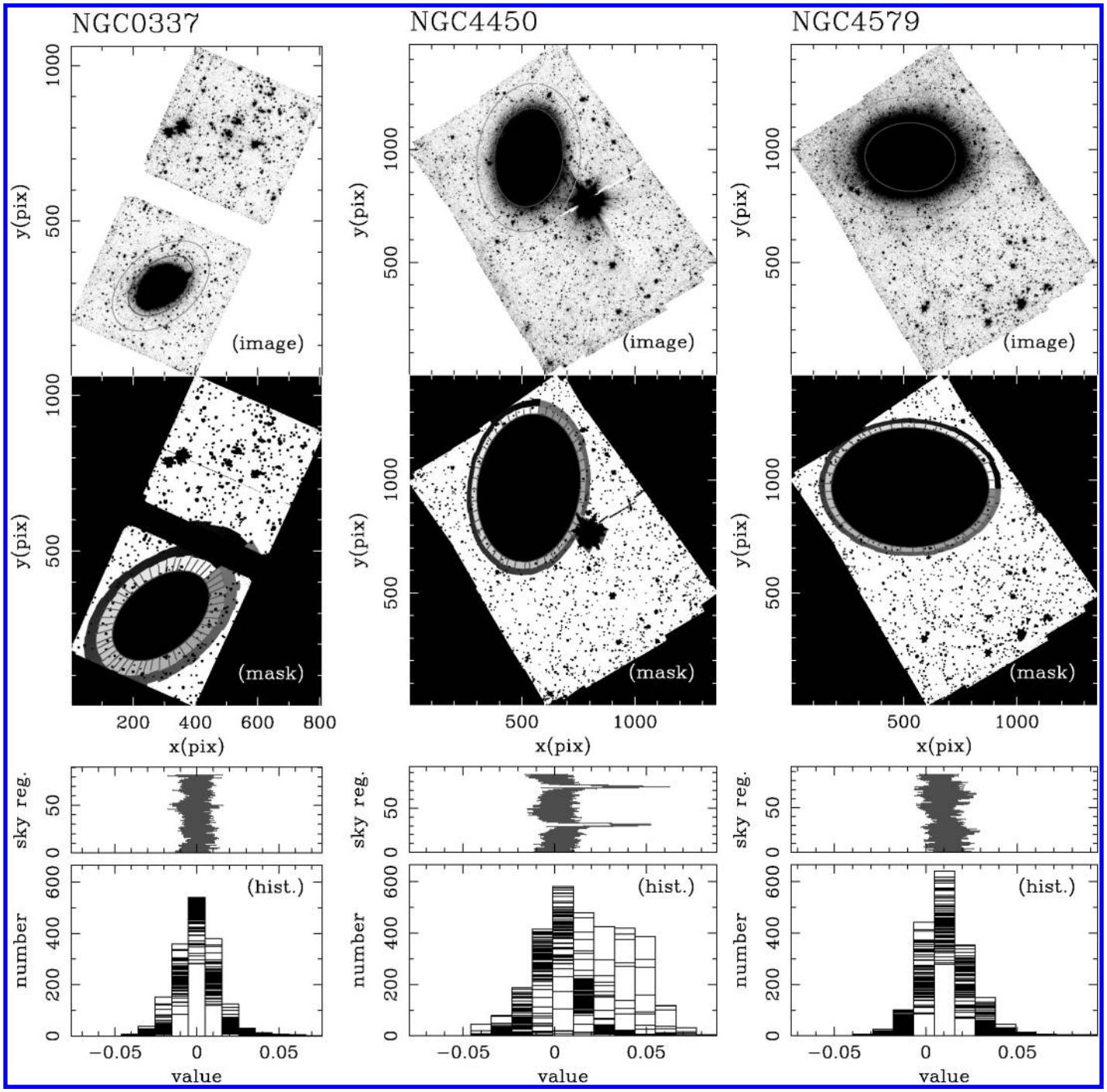

FIG. 4.—Results of the determination of the sky background for the S^{4}G galaxies NGC 0337, NGC 4450, and NGC4579. *Top row*: Results for the IRAC 3.6 μm image for each galaxy. The D_{25} ellipse is shown and the inner edge of the annulus from where we begin to estimate the sky is shown. *Second row*: The elliptical annuli used to compute the sky background are shown. The segments indicate the 45 regions of the inner annulus. The outer annulus used to trace the gradient is shown shaded by the grayscale annulus. The changing shade from light gray to black corresponds to the 45 regions of the outer annulus. In this row all the masked pixels are shown in black, but note that the black color of the outer annulus does not mean that these regions are masked. *Third row*: The median and standard deviation for each of the 90 sky boxes is shown here. *Bottom row*: A histogram of the pixel values within each of the 90 sky boxes is shown in this panel. See the electronic edition of the *PASP* for a color version of this figure.

figure, we show an example case for NGC 4450, where the median sky in some of the boxes is affected by the bleeding of flux from a (masked) but saturated nearby bright field star. In such cases we ignore the affected pixels or move the annuli further out to get the best estimate for the background. Finally, we use the standard deviation obtained from the 90 sky boxes with the average standard deviation within each box to estimate the contribution of the low-frequency flat-fielding errors and possible additions to the total error budget in the background determination.

The typical sky brightness level is fainter than $26(\mathrm{AB})$ mag arcsec^{-2} at 3.6 and 4.5 μm. The Poisson noise from the galaxy dominates the total error budget in the central regions, while errors in the sky background are the main source of uncertainty in the outer parts. Large-scale background errors can be particularly significant in galaxies with large apparent sizes. However, in the fainter outer parts, the noise is significantly reduced from azimuthally averaging over a large number of pixels in the outer galaxy—we are therefore able to measure the galaxy profiles well below the typical sky brightness. The typical S/N for a S^{4}G galaxy at the canonical $\mu_{3.6\mu} = 26.5(\mathrm{AB})$ mag arcsec^{-2} is greater than 3.

The images resulting from Pipeline 1 are calibrated in units of MJy sr^{-1}. The conversion from MJy sr^{-1} to AB magnitudes is such that the zero point to convert fluxes in jansky to magnitudes does not vary with wavelength (Oke 1974):

$$m_{\mathrm{AB}}(\mathrm{mag}) = -2.5 \log F_\nu(\mathrm{Jy}) + 8.9. \quad (1)$$

From this definition one can derive the corresponding expression for surface brightness:

$$\mu_{\mathrm{AB}}(\mathrm{mag}) = -2.5 \log I_\nu(\mathrm{MJy\ sr^{-1}}) + 20.472. \quad (2)$$

5.3.1. P3: Measuring the Galaxy Host Properties

After the sky level has been properly measured, we use the IRAF routine `ellipse` to determine the radial profiles of intensity, surface brightness, ellipticity, and position angle for all galaxies in both bands. The center is determined using `imcenter` and kept fixed during the fit, whereas the ellipticity and position angle are left as free parameters. We generate profiles with two different radial resolutions, by incrementing the semimajor axis in 2″ and 6″ at each step, respectively. The latter profiles have a coarser resolution and a better S/N—these are used to measure the RC3-like parameters. The low- and high-frequency sky background errors described previously, together with the Poisson noise of the source along each isophote, are considered together in the final error budget of the surface photometry at each radius (see Gil de Paz et al. 2005; Muñoz-Mateos et al. 2009). The errors in the position angle and ellipticity at each radius are computed by the ellipse task from the rms of the pixel values along each fitted isophote. The corresponding errors for the values of these geometrical parameters at 25.5 and $26.5(\mathrm{AB})$ mag arcsec^{-2} are interpolated between the corresponding adjacent values. The error in the semimajor axis is computed from the change in the radius affected by moving the surface brightness profile by the measured errors and an additional 10% error added in quadrature to the measured errors. The 10% error is an estimate of the aperture correction uncertainty as estimated by the Spitzer Science Center instrument team. We compute the error in the semimajor axis for each galaxy. Sample results for NGC 0337 and NGC 4579 are shown in Figure 4 and noted in Table 2. For NGC 4450, the scattered light from a background star strongly affects the computation of the surface brightness error and therefore the error in the semimajor axis is unrealistic. In such cases, the error in the semimajor axis can be assumed to be the median semimajor axis error in the S^{4}G sample. The maximum error in the determination of the semimajor axis is 6″, which is the step size of the coarse-resolution fitting procedure.

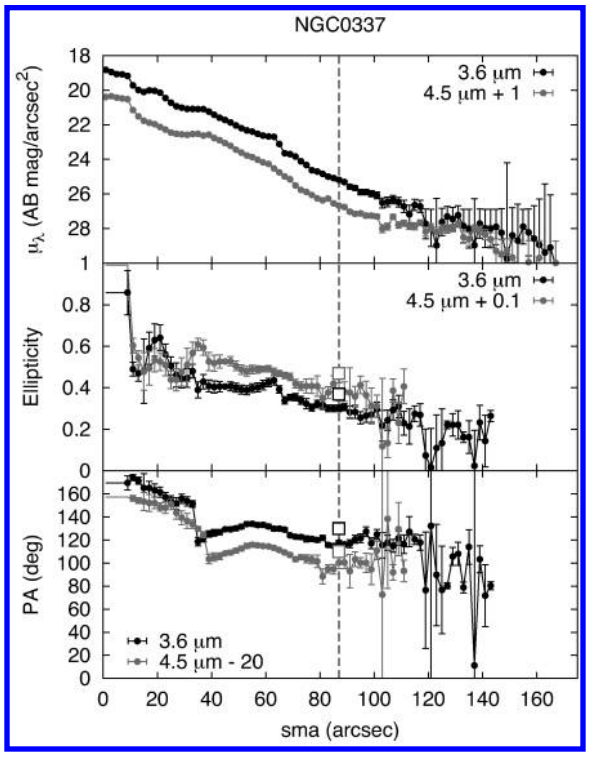

FIG. 5.—Surface photometry results for the S^{4}G galaxy NGC 0337. *Top*: Surface brightness profiles for 3.6 μm (black filled circles) and 4.5 μm + 1 mag (gray filled circles). The vertical dashed line shows the position of the B-band D_{25} major axis radius. *Middle*: Variation of the ellipticity of the best-fitting isophote with the radius. For the sake of clarity we have applied an offset of 0.1 to the 4.5 μm profile. *Bottom*: Position angle of the best-fitting isophote as a function of radius. Note the 20° offset applied to the 4.5 μm profile. The boxes drawn at the position of the D_{25} major-axis radius in the latter two panels indicate the ellipticity and position angle listed in the RC3 catalog, respectively.

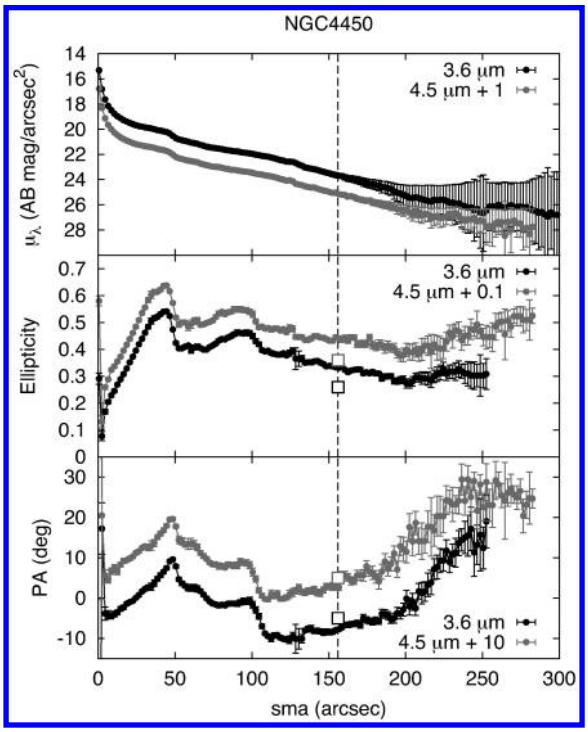

FIG. 6.—The same as Fig. 5, for NGC 4450.

In Figures 5, 6, and 7 we show three sample sets of profiles for three galaxies in the sample: NGC 0337 (SBd), NGC 4450 (SAab), and NGC 4579 (SABb). The basic RC3-like galaxy

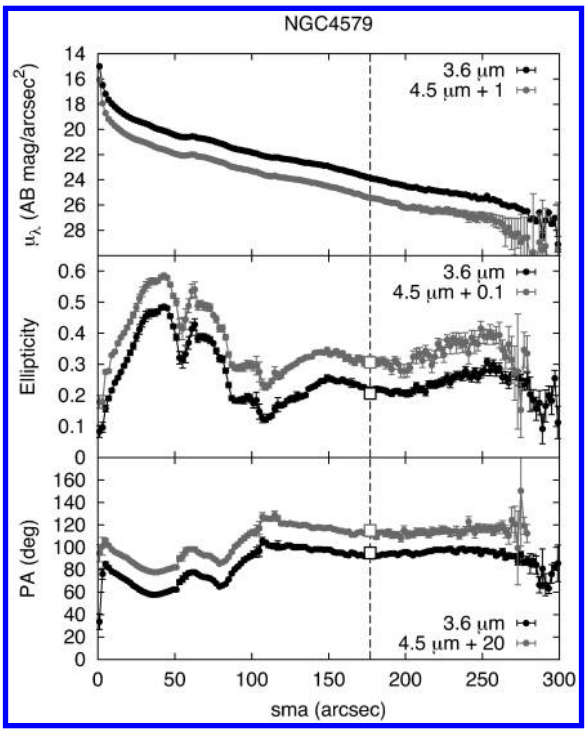

FIG. 7.—The same as Fig. 5, for NGC 4579.

properties (semimajor axis, axial ratio, and position angle) are tabulated at the levels of 25.5 and $26.5(\mathrm{AB})$ mag arcsec^{-2} in both the 3.6 μm and the 4.5 μm images and are quoted in Table 2.

Along with the surface photometry we also measure the curve of growth (e.g., Muñoz-Mateos et al. 2009; Gil de Paz et al. 2007) with the integrated flux up to each radius. By fitting the accumulated magnitude as a function of the magnitude gradient at each point we obtain the asymptotic magnitude as the y-intercept of that fit (see Gil de Paz et al. 2007). Once the total magnitude is known, it is straightforward to locate the radii containing a given percentage of the total galaxy luminosity, from which concentration indices can be determined. In Table 3 we quote the asymptotic magnitudes of the three sample galaxies considered here, together with the C_{31} (de Vaucouleurs et al. 1977) and C_{42} (Kent 1985) concentration indices.

5.4. S^{4}G Pipeline 4

In Pipeline 4, we decompose the two-dimensional stellar distribution in each galaxy into different subcomponents using the version 3 of GALFIT (Peng et al. 2002, 2010). GALFIT is a parametric fitting algorithm that offers a large flexibility on the fitted models; the optimal solution for the model parameters is found with the Levenberg-Marquardt algorithm, performing nonlinear least-squares χ^2 minimization of the difference between observed and model images. For our pipeline, we could have also used bulge/disk decomposition analysis (BUDDA; Gadotti 2008) and bulge/disk/bar (BDBAR; Laurikainen et al. 2005). We tested all three algorithms using a set of galaxy images and verified that GALFIT produces the same results as BUDDA and BDBAR if the three codes are run with the same set of input images, models, and initial parameters. We chose GALFIT because it is currently the most sophisticated algorithm and also well known by a large portion of the astronomical community. Other studies in which software was developed for similar purposes include Simard (1998), Pignatelli et al. (2006), and Méndez-Abreu et al. (2008).

To simplify the use of GALFIT for a large number of cases, a set of new IDL-based tools has been created (GALFIDL). The tools include automatic creation of the input files for decompositions, containing reasonable first guesses for the initial parameters based on P3 products, and routines for running and visualizing the decompositions. GALFIDL will be available to the community concurrently with the publication of the data and the GALFIT analyses.[28]

As a standard part of the pipeline analysis, decompositions include bulges and disks (and, if appropriate, bars, nuclear components, and, in some cases, multiple exponential disks). Taking into account that decompositions, particularly at high redshift,

[28] An overview of these procedures is already available at http://cc.oulu.fi/~hsalo/galfidl.html.

TABLE 2
SAMPLE RC3-LIKE PARAMETERS

		36 μm			4.5 μm		
Galaxy	μ	Semimajor axis	Ellipticity	Position angle	Semimajor axis	Ellipticity	Position angle
NGC 0337	25.5	90.6 ± 1.5	0.287 ± 0.018	118.4 ± 2.0	84.1 ± 1.3	0.278 ± 0.037	118.5 ± 4.5
NGC 0337	26.5	110.4 ± 4.7	0.270 ± 0.027	119.8 ± 3.2	106.9 ± 1.3	0.287 ± 0.055	123.8 ± 7.1
NGC 4450	25.5	209.0 ± 6	0.293 ± 0.016	1.4 ± 1.8	199.9 ± 6	0.293 ± 0.020	3.2 ± 2.3
NGC 4450	26.5	253.0 ± 6	0.336 ± 0.048	19.8 ± 5.1	$266.7 \pm \ldots$	0.418 ± 0.026	18.1 ± 2.3
NGC 4579	25.5	256.0 ± 2.6	0.295 ± 0.011	95.2 ± 1.2	229.0 ± 2.6	0.268 ± 0.018	95.5 ± 2.2
NGC 4579	26.5	278.6 ± 17	0.251 ± 0.018	78.6 ± 2.4	263.4 ± 12	0.282 ± 0.027	98.3 ± 3.4

NOTE.—RC3-like parameters for three sample galaxies. For each galaxy and band we quote the semimajor axis (in arcseconds), the ellipticity, and the position angle (in degrees) at two levels of surface brightness: 25.5 and 26.5(AB) mag arcsec^{-2}. The error in the semimajor axis is measured by noting the change in the corresponding radius when the surface brightness profiles are shifted up and down by the local measurement error plus 10% additional error, which is the maximum expected from any scattered light on the detector. For NGC 4450, the error cannot be measured due to contamination from a background star and is therefore set to the maximum error, 6″, as discussed in the text. The errors in the ellipticity and position angle are from the ellipse fitting and reflect the rms in the formal fit of the corresponding isophote. These errors are significantly larger than any error introduced by the shifting the profiles to measure the error in semimajor axis.

are often made in a simpler manner, we also compute the two-component bulge/disk decompositions and one-component Sérsic function fits. A decomposition for NGC 1097 is shown in Figures 8 and 9: the five-component model includes an exponential disk, a Sérsic function for the bulge, and a Ferrers function for the bar. The galaxy has an extremely prominent nuclear ring, which is fit using a Gaussian function, and a nuclear point source using the corresponding PSF. Without deep, almost dust-free, observations (such as those in S^{4}G), the measurement of bulge structural parameters (such as like shape, size, and profile), might be compromised in some cases if the quantification of underlying structures (such as the disks, bars, and rings) is inaccurate. GALFIT 3.0 allows for even more sophisticated decompositions, which will be made for selected subsamples of S^{4}G galaxies. For example, it is possible to add more components, or one may want to fit the spiral arms, an example of which is shown in Figure 10.

6. S^{4}G SCIENCE INVESTIGATIONS

In this section we highlight some preliminary results from a number of science investigations that are and will be carried out by the S^{4}G team. We also discuss possible studies that will be enabled by the S^{4}G data set.

6.1. The Faint Outskirts of Galaxies

A major area of study for S^{4}G is a quantitative analysis of stellar structures in the faint outer regions of galaxies, where the stellar surface density we trace is extremely low and comparable with, or lower than, the atomic gas reservoir. Deep optical studies have already shown that in a majority of spiral galaxies, the outer disks exhibit a secondary exponential component. Stellar disks appear to extend beyond $1.5 \times D_{25}$ (e.g., Pohlen & Trujillo 2006; Erwin et al. 2008) with truncated or antitruncated profiles. *GALEX* (Martin et al. 2005) has found extended UV disks even farther out, where it was assumed only H I gas existed (e.g., Gil de Paz et al. 2005; Thilker et al. 2005, 2007; Muñoz-Mateos et al. 2007; Zaritsky & Christlein 2007). Not only is S^{4}G significantly deeper than the previous optical data, but it also traces the stellar profiles into the H I disk of the galaxy—in over 800 S^{4}G galaxies, we image an area greater than $3D_{25}$.

Another observation that has been much debated is the break between the inner and outer exponential profiles (e.g., Bakos et al. 2008; Azzollini et al. 2008). With S^{4}G we are measuring the break radius and comparing it with the disk size and mass. The S^{4}G catalog of these breaks will provide strong quantitative constraints for galaxy evolutionary models. In particular, this

TABLE 3
MAGNITUDES AND CONCENTRATION INDICES FOR S^{4}G GALAXIES

	3.6 μm			4.5 μm		
Galaxy	Magnitude (AB)	C_{31}	C_{42}	Magnitude (AB)	C_{31}	C_{42}
NGC 0337	11.432 ± 0.001	2.67	2.74	11.888 ± 0.002	2.82	2.90
NGC 4450	9.630 ± 0.001	4.58	4.17	10.112 ± 0.001	4.56	4.16
NGC4579	9.083 ± 0.001	5.29	4.54	9.564 ± 0.001	5.60	4.71

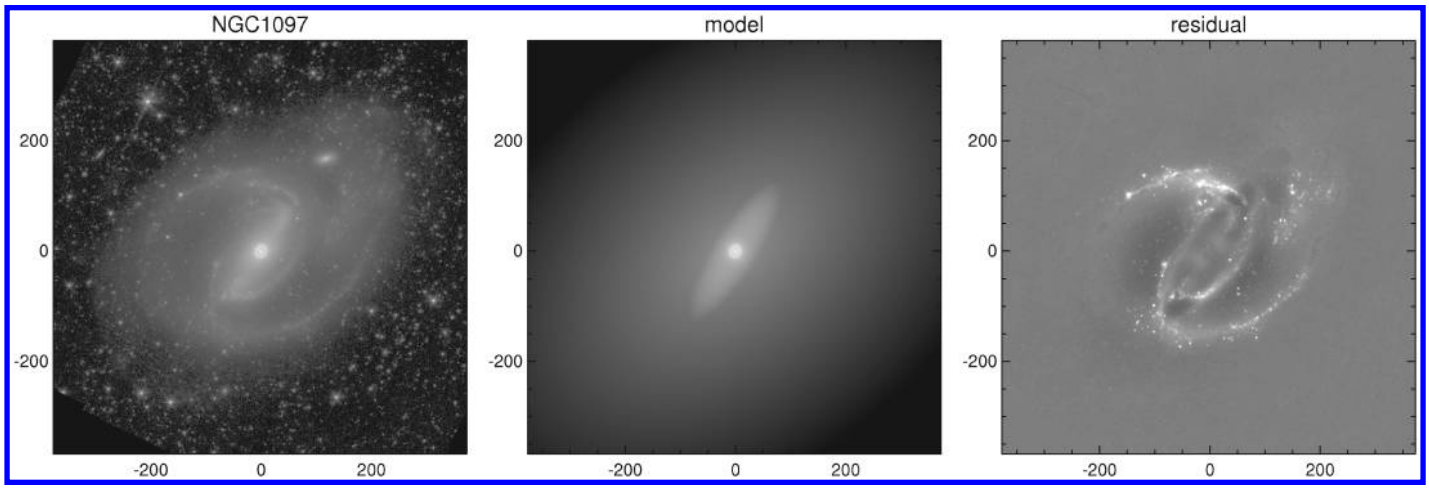

FIG. 8.—Five-component decomposition model for NGC 1097. The panels show the observed 3.6 μm image (*left*), the model image (*middle*), and the normalized residual image (OBS-MODEL)/MODEL (*right*). North is up and east is to the left, per the usual conventions, and the units are in arcseconds. The decomposition includes bulge, disk, bar, central point source, and nuclear ring components, as illustrated in Fig 9. Note how the residual image, emphasizes the outer spiral and the inner ring structures.

catalog will be key to quantifying the possible role of radial stellar migration in shaping the outskirts of disks (Roškar et al. 2008; Sánchez-Blázquez et al. 2009).

In elliptical galaxies, deep optical observations have revealed the presence of faint tidal tail and shell-like structures (e.g., Bennert et al. 2008; Canalizo et al. 2007). S^{4}G contains 188 ellipticals and lenticulars—with this set and the S^{4}G depth, we are quantifying the frequency and mass of shells and other debris features in the outskirts of ellipticals and lenticulars.

6.2. Bulges: Classical, Disk-like, Boxy/Peanut

Bulges are an inhomogeneous class of objects, and different types have been proposed in the literature (Kormendy & Kennicutt 2004; Athanassoula 2005). Kormendy & Kennicutt (2004) distinguish bulges from pseudobulges, while Athanassoula (2005) distinguishes three categories: classical bulges; boxy/peanut bulges, which are a part of a bar; and disklike bulges, formed out of disk material. Several studies have analyzed their observational properties and compared them with N-body models (e.g. Kuijken & Merrifield 1995; Carollo et al. 1997; Bureau & Freeman 1999; Erwin et al. 2003; Bureau & Athanassoula 2005; Fisher 2006; Drory & Fisher 2007; Fisher & Drory 2008; Gadotti 2009). Even in lenticular galaxies there seems to be evidence for disklike bulges, based on structural decompositions (e.g., Laurikainen et al. 2005, 2007; Gadotti 2008; Graham & Worley 2008) and kinematics (e.g., Peletier et al. 2007; Falcón-Barroso et al. 2006). But until now few studies have analyzed the structural properties of bulges in a large number of galaxies; none have done it in a sample as large and deep as S^{4}G. Moreover, S^{4}G encompasses a range of large-scale structures, allowing us to examine the environmental influences on the formation of bulges. This may have important implications, since massive bulges are expected to form from mergers.

From a preliminary analysis of the S^{4}G data, Buta et al. (2010) are finding that many late-type ellipticals in the RC3 have disks and thus should instead be classified as S0s, consistent with

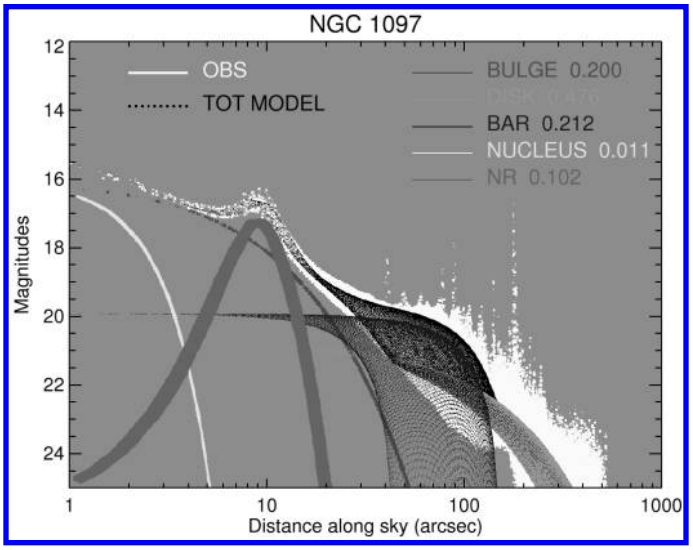

FIG. 9.—The different subcomponents of the NGC1097 fit in Fig. 8. The white dots show the magnitude of each pixel of the observed image as a function of distance from the galaxy center along the sky plane, while the dark points indicate the total model. The different shades indicate different subcomponents: the numbers after the labels indicate the relative contribution of the component to the total model flux. In this type of plot, axially symmetric components appear as curves, while nonaxisymmetric components (i.e., the bar) fill a region confined by their major and minor axes profiles. Similar plots have been used to visualize BDBAR (Laurikainen et al. 2005) and BUDDA (Gadotti 2008) decompositions. See the electronic edition of the *PASP* for a color version of this figure.

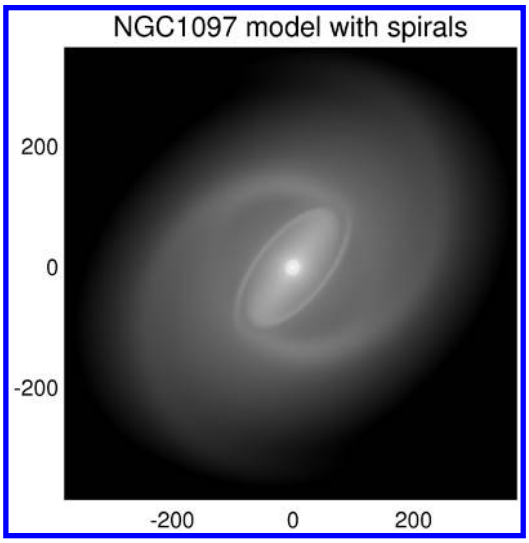

FIG. 10.—Illustration of the capabilities of GALFIT 3.0: a decomposition for NGC 1097, including spiral subcomponents. Although for many scientific purposes it is reasonable to use parametric functions such as Sérsic or Ferrers functions for fitting structural components, GALFIT also allows modeling of curved or irregular structures. As an illustration of modeling where the spiral arms form part of the decomposition, a model for NGC 1097 is shown—it shows a remarkable resemblance to the observed image. We caution the reader, however, that since the residuals contain contributions from partially modeled spiral arms, the model parameters output by GALFIT are not necessarily ideal for the study of faint structures in galaxies.

other deep near-infrared studies (Laurikainen et al. 2010). With the S^{4}G data we will examine how common the disk structure is in all types of ellipticals.

Finally, the extremely deep data from S^{4}G allows us to best determine the structural properties of the bulge component—in shallower data, estimates of shape, size, and profile are uncertain when measurements of underlying components such as disks, bars, and rings are imprecise. As described in § 5.4, the S^{4}G project is carrying out detailed decomposition of all the galaxies and expects to compile the most detailed database of bulges of all kinds. The combined advantages of the S^{4}G data (deep and insensitive to dust attenuation) and the uniform reduction pipeline (careful and detailed structural analysis) will allow for a suitable examination of galaxies with composite bulges: i.e., galaxies hosting more than one bulge category (e.g., Erwin et al. 2003; Kormendy & Barentine 2009; Nowak et al. 2010). The spatial resolution of our survey is adequate for resolving typical bulges (our resolution is ∼100 pc at the median distance of the survey volume), but is inadequate for precise measurements of the bulge structure from the inability to resolve compact nuclear structures that are often present at the centers of galaxies. These unresolved point sources affect the values of Sérsic parameters, which, on average, are overestimated in ground-based optical images, compared with *Hubble Space Telescope* studies (e.g., Carollo et al. 1997; Balcells et al. 2003). We also expect that the reduced dust extinction may reveal triaxial structures in bulges and thus allow us to probe beyond the standard symmetric Sérsic fits.

6.3. Bars

Stellar bars are dynamically important structures in galaxies. A bar-induced gas flow leads to a number of evolutionary effects from the triggering of circumnuclear starbursts to the buildup of bulges (Scoville & Hersh 1979; Simkin et al. 1980; Zaritsky & Lo 1986; Athanassoula 1992; Friedli & Benz 1993; Martin & Roy 1994; Friedli & Benz 1995; Sakamoto et al. 1999; Sheth et al. 2000, 2002, 2005). The cosmological redshift evolution of the bar fraction is also an important signpost of the growth and dynamic maturity of galaxies (e.g., Abraham et al. 1999; Sheth et al. 2003; Jogee et al. 2004; Elmegreen et al. 2004; Sheth et al. 2008). Whereas the previous smaller and shallower studies gave mixed results for the change in the bar fraction with redshift, Sheth et al. (2008) show that not only does the overall bar fraction in disk galaxies decline significantly over the last seven billion years, but also that the decline depends on the galaxy type. They show that the formation and evolution of bars is strongly correlated with the host galaxy mass, bulge dominance, and presumably their dark-matter halo. The S^{4}G data are critical to establish the precise local frequency of bars and its variation with galaxy type. The data also provide a measurement of the light fraction in the bar component (e.g., Durbala et al. 2008; Gadotti 2008; Weinzirl et al. 2009) and accurate measurements of properties such as the bar length, shape, and ellipticity (e.g., Menéndez-Delmestre et al. 2007; Erwin 2005; Gadotti 2010). Several techniques may be used to derive bar strengths, based on calculating bar torques (Laurikainen & Salo 2002; Buta et al. 2003) and estimating the bar-spiral arm contrast (Elmegreen & Elmegreen 1985). Analysis of the relative Fourier intensity profiles of bars is compared with models of the evolution of barred galaxies (e.g., Athanassoula & Misiriotis 2002; Debattista et al. 2004) to constrain the history of their evolution and interaction with their dark-matter halo (Athanassoula 2003).

Another study of interest is the presence of secondary or nuclear bars that may be responsible for feeding the central black holes and/or stellar clusters (Shlosman et al. 1990). The S^{4}G observations, unaffected by the high and patchy extinction often present in galactic centers, allow us to detect all nuclear bars with sizes of $r > 500$ pc (our resolution, $2'' \sim 200$ pc at the median distance of S^{4}G) in galaxies of all types.

6.4. Galactic Rings

Outer rings are large, optically low, surface brightness features that dominate the outer disks of some early-type barred and weakly barred galaxies (see the review by Buta & Combes 1996). The properties of the rings constrain their formation epoch, the dynamical time-scale at their respective radii, and the evolution of the bar pattern speed (e.g., Athanassoula

2003). Finding outer rings around unbarred galaxies is also of great interest, because it would suggest that some unbarred galaxies may in fact be highly evolved former barred galaxies. Whereas ground-based near-IR imaging is rarely deep enough to detect outer rings reliably to study their stellar populations, colors, and other characteristics, the S^{4}G data will allow us to not only detect many new outer rings, but also to make a complete census of these features in normal galaxies and to measure their stellar mass, shape, width, and ellipticity. Likewise, S^{4}G provides an unprecedented view of circumnuclear and inner rings, which are typically found in barred spirals. These rings should have a broad underlying older stellar population background as they evolve, and it is this type of feature we will see in the S^{4}G data.

6.5. Spiral Arms

A systematic study of spiral arm amplitudes as a function of radius at 3.6 and 4.5 μm, free of confusing effects from dust extinction, promises to initiate a new set of spiral arm studies. Although the discrepancies in the classical density wave model were solved with the swing amplification theory (Toomre 1981), there has been very little testing of this theory with observations. Modal studies by Bertin et al. (1989a, 1989b) predict that there should be amplitude variations along the arms from resonances between inward- and outward-moving spiral waves, and the precise amplitude variations have been modeled (Elmegreen & Elmegreen 1984; Elmegreen et al. 1989; Elmegreen & Thomasson 1993; Regan & Elmegreen 1997). Most recently, a new theory has been proposed for the formation of rings and spiral arms, which argues in favor of chaotic orbits, confined by invariant manifolds emanating from the L1 and L2 Lagrangian points of a bar (Romero-Gómez et al. 2007). Several comparisons between the results of this theory and observations have been carried out successfully (Athanassoula et al. 2009a, 2009b) and several more will be possible with the S^{4}G database. S^{4}G will cover the full range of galaxies with varying spiral arm strengths and galactic structures. In Figure 11, we show a

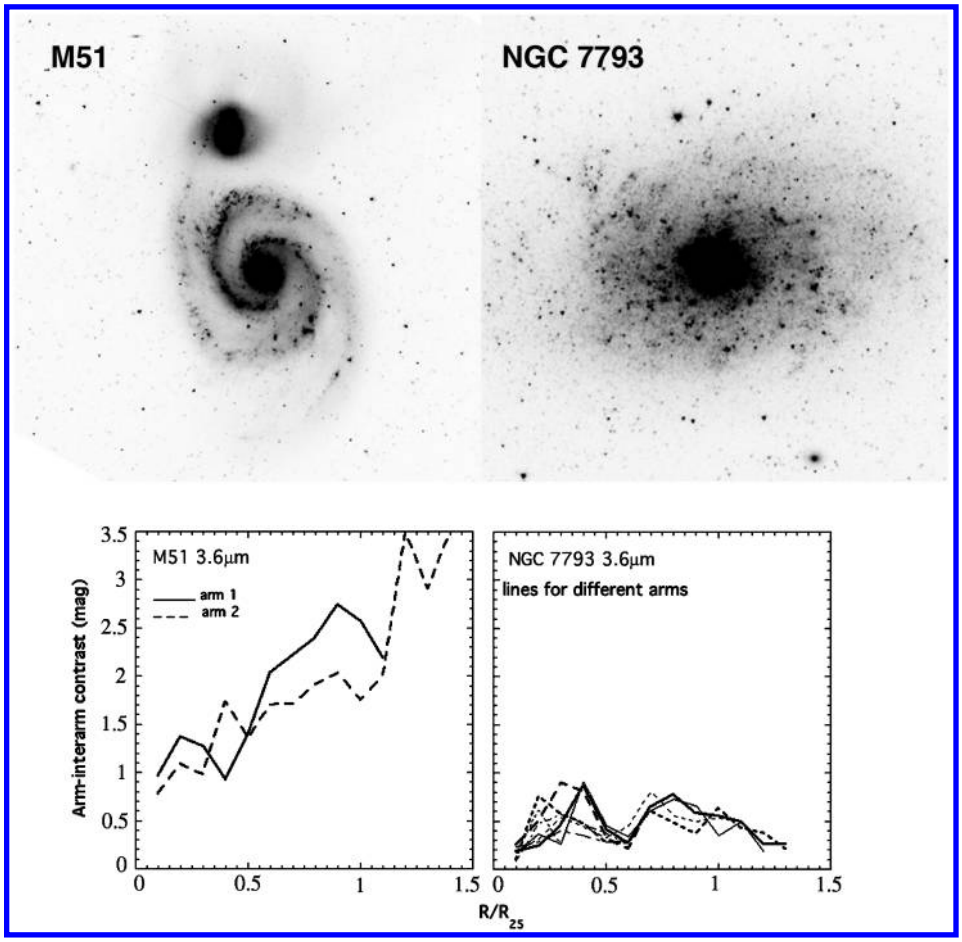

FIG. 11.—Preliminary analysis of the arm-interarm ratios computed for a flocculent spiral, NGC 7793, and a grand-design spiral, M51, from the S^{4}G 3.6 μm data. Note the increasing contrast in the grand-design galaxy compared with the flocculent galaxy. Detailed analysis of the stellar density variations will shed important light on spiral density wave theories.

preliminary result of the type of analysis that is possible with the S^{4}G data. In this figure we show the arm-interarm contrast measured from the 3.6 μm S^{4}G images for NGC 7793, a flocculent galaxy, in contrast with M51, a grand-design spiral galaxy (see a model for amplitude variation of M51 in Salo & Laurikainen 2000b). The contrasts are measured beyond R_{25}, further than in previous optical studies. The spiral structure traced in the 3.6 μm band is different in detail from the optical images, but still shows weak arms in NGC 7793 and increasingly stronger arms in M51. We will carry out a detailed analysis of spiral arm amplitudes and variations and compare the observational data with the models.

For the NGC 5194 (M51) system, there may well be a connection between the spiral structure and the presence of the companion (NGC 5195). Indeed, detailed H I observations by Rots et al. (1990) show the presence of a long tail, which emanates from the west side of the galaxy, running south of the spiral arm visible in the S^{4}G image, and turning up toward the north, further eastward. The H I kinematics are very difficult to model with an interaction involving a single passage, but Salo & Laurikainen (2000a, 2000b) propose a model with a second passage (Fig. 12), which gives a better fit to some of the aspects of the observations. The inner spiral structure in the main spiral is then amplified by the action of the companion, and wave interference causes amplitude modulations, which are well reproduced in the S^{4}G observations (Fig. 13). This shows the interest of the S^{4}G data for detailed modeling of the dynamics of individual galaxies.

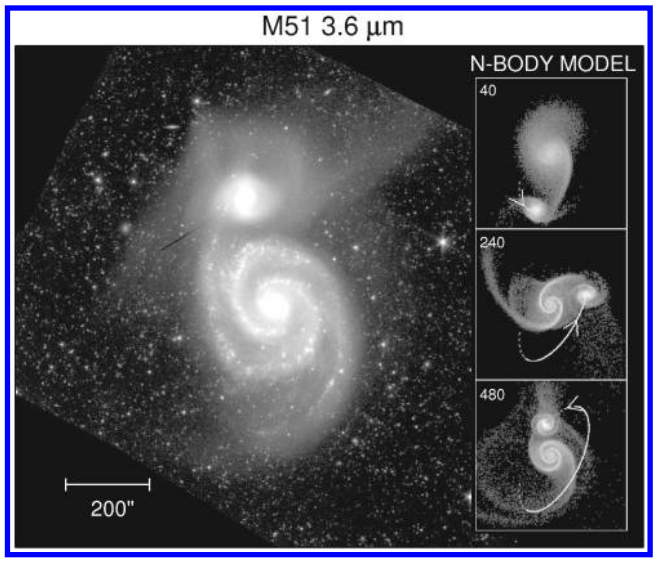

FIG. 12.—Comparison of the M51 3.6 μm image with the N-body simulation model of Salo & Laurikainen (2000b,2000a). The right-hand column shows the simulation at 40, 240, and 480 Myr from the top to the bottom panels, respectively. In the model the near-IR and rotation curve data existing at the time were used for setting up the initial disk and halo models. The simulation creates an outer southern tail when the companion (with mass ratio 0.55) crosses the primary disk toward the observer about 480 Myr ago. To obtain the observed apparent counter-rotating H I kinematics, the tail has a tilt of nearly 40° with respect to the inner disk. The most recent disk plane crossing about 100 Myr ago is responsible for the ejecta north of the companion, drawn from the primary disk, and visible in the S^{4}G image. During the prolonged interaction the tidal wave induced by the direct perturbation is able to propagate to the central regions, consistent with the inner spiral structure described by Zaritsky et al. (1993).

6.6. Early-Type Galaxies and Dwarfs

S^{4}G contains 188 galaxies of T-type <0 and therefore constitutes one of the largest and most homogeneous mid-infrared data sets for early-type galaxies. The shapes of ellipticals and lenticulars may reflect different evolutionary paths, with wet mergers leading to disky shapes and dry mergers leading to boxy profiles (Naab et al. 2006; Pasquali et al. 2007; Kang et al. 2007). In addition, Kormendy et al. (2009) show that deep imaging can reveal departures from the Sérsic profiles in elliptical galaxies, which are diagnostics of their formation. They found a dichotomy in which ellipticals that have cuspy cores at their inner radii can be separated from those that show an excess of light at the center. The S^{4}G data offer us a unique opportunity to revisit the frequency of the different shapes and profiles as a function of stellar mass and environment, free of dust obscuration effects.

Although dwarfs are the most abundant type of galaxy in the universe, their low surface brightnesses of typically $\mu_B > 22$ mag arcsec^{-2} have restricted detailed observations of these stellar systems. In particular, the characterization of the

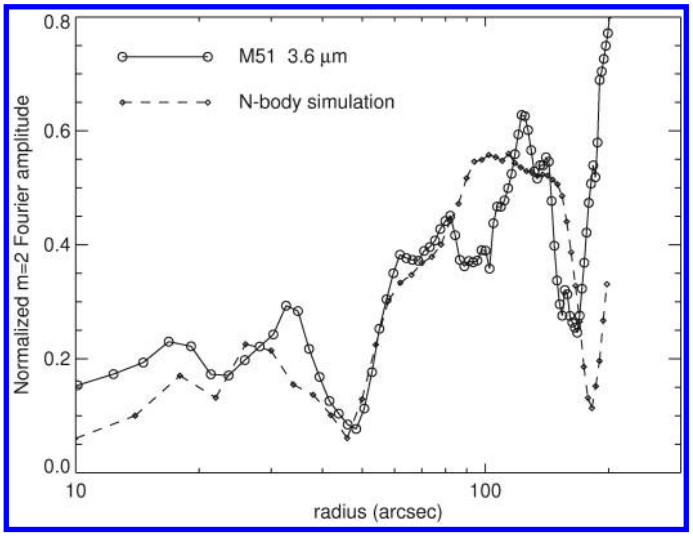

FIG. 13.—Comparison of the $m = 2$ Fourier amplitude profile of M51 extracted from S^{4}G 3.6 μm image with the N-body simulations of Salo & Laurikainen (2000b,2000a). The simulation corresponds to the final snapshot of Fig. 12. The outermost observed minimum at $r \approx 180''$ is related to the change of the curvature of arms: in simulations a similar feature marks the region where the self-gravity sustained spiral wave separates from purely tidal outer structure. In the model the minima at $r \approx 40$ and 20" are amplitude modulations, which arise due to interference between separate inward-propagating tidal wave packets. See also Fig. 11 for M51 at $R_{25} \approx 300''$

underlying stellar structure in these faint galaxies still remains largely unexplored. Using an absolute magnitude criterion of $M_B > -17$, we have identified a preliminary sample of 206 dwarf galaxies in S^{4}G. The sample includes 87 late-type DDO dwarfs previously unobserved with *Spitzer*, to complement the 48 that have been observed. The S^{4}G dwarfs therefore constitute a representative sample of nearby dwarf galaxies in which to study the properties of the underlying stellar component.

Dwarf galaxies in S^{4}G allow for a detailed analysis of the underlying stellar disk in both the 3.6 and 4.5 μm data. By deriving the radial scale lengths for these galaxies, more insight can be gained into the evolutionary link between dwarfs and their giant counterparts. At the same time, the relatively large sample of dwarfs in S^{4}G gives a unique opportunity to look at how these parameters may vary with environment. We can also derive stellar masses for the dwarfs that will be used to assess their stellar mass to dark-matter ratio and will likely provide crucial evidence to the long-standing debate of whether these galaxies are truly dark-matter-dominated systems (see, e.g., Strigari et al. 2008).

In addition to these areas, there are at least three other main areas of astrophysics that these data will address uniquely: the reported absence of bulges in some disk galaxies, the vertical stellar structure, and the Tully-Fisher relationship. There is also likely to be significant amounts of spin-off science for S^{4}G with its large and accurate inventory of mass and galactic structure in the nearby universe: e.g., the relationship between the Tully-Fisher relationship and properties of the fundamental plane (e.g., Zaritsky et al. 2008), dust heating in outer disks, the interaction/merger fraction from a study of the debris around these galaxies, and diagnosis of AGN activity from tracing hot dust very close to the AGN from the 3.6–4.5 color.

7. DATA RELEASE AND TEAM POLICY

The S^{4}G team is committed to releasing all of the reduced data upon publication of all S^{4}G data sets from each of the pipelines. We expect the science-ready images from Pipeline 1, the masks from Pipeline 2, the galaxy properties and profiles from Pipeline 3, and the input and output files from Pipeline 4 (including the mask, sigma images, images without NaN values, and the GALFIT input and output parameter files) to be released on a staggered schedule using the NASA/IPAC Extragalactic Database (NED) or NASA/IPAC Infrared Science Archive (IRSA) for long-term use by the community. Currently, the products of each of the pipelines are expected to be released in journals upon verification of their quality, which will be ongoing and will occur as part of the various scientific investigations conducted by the team. We expect that some of the data and pipeline may need to be refined or enhanced in the future. As the data are still being acquired (data acquisition is expected to be complete in 2011) and analyzed, our earliest release date for the science-ready images (P1 products) for the entire S^{4}G data is not expected at least until 2012, and the supplemental articles for the products from the other pipelines are expected to follow within a year after the Pipeline 1 supplemental article. In the meantime, to allow for maximum use of the data for science by the larger community, the collaboration has agreed on an open-door policy, whereby any member of the astronomical community may join the team temporarily as a guest and pursue any type of science. The uses of the data, publication policies, and authorship on articles are clearly defined in our policy statement.[29] This statement is adopted by the S^{4}G team and all of its guests. Interested members of the astronomical community are invited to read the policy and contact the Principal Investigator or an S^{4}G member to discuss the possibilities of joining the team.

The noteworthy point of this policy is that our team has agreed to avoid carving out large science categories or areas, to encourage the maximum use of the data within the team, and within the larger community, for any science that may be possible with these data. Our philosophy is that if multiple people are interested in a topic but want to work in separate teams, then we will encourage both teams to collaborate and address the scientific problems in independent but parallel investigations.

8. SUMMARY

S^{4}G will provide the deepest, largest, and most homogenous data set of nearby galaxies at 3.6 and 4.5 μm. The spatial resolution will be unmatched at these wavelengths, $\sim 2''$, which is ideal for comparisons with ground-based optical and near-IR observations, as well as MeerKAT (Karoo Array Telescope), eVLA (Expanded Very Large Array), ALMA (Atacama Large Millimeter/Submillimeter Array), and other future large radio array surveys. The sample of 2331 galaxies includes most morphological types and masses. The images will give an unparalleled view of stellar mass distributions and faint peripheral structures. All of the galaxies, as well as many additional galaxies from the *Spitzer* archives, will be reduced in the same way, giving data products that span the full range from science-ready images to measurements of global galaxy properties and individual components. S^{4}G is designed to be a useful reference for many years to come. It will contain the best available mid-infrared data for individual galaxies and will be among the most complete surveys for statistical studies. It will be useful to study the origin and evolution of galaxies and their dynamical components and to supplement observations of nearby galaxies at other wavelengths.

The authors thank the referee for useful comments and suggestions that greatly helped improve this article. We are also grateful to the dedicated staff at the Spitzer Science Center for their support and help with the planning and execution of

[29] Available at http://www.cv.nrao.edu/~ksheth/s4gpolicy.pdf.

this legacy exploration program. K. S. would like to thank L. Armus, E. Bell, S. Carey, E. Churchwell, M. Dickinson, G. Helou, N. Scoville, and J. Stauffer for sharing their experiences in leading large teams. A. G. d. P. and J. C. M. M. are partially financed by the Spanish Programa Nacional de Astronomía y Astrofísica under grants AyA2006-02358 and AyA2009-10368. A. G. d. P. is also financed by the Spanish Ramón y Cajal program. J. C. M. M. acknowledges the receipt of a Formación del Profesorado Universitario fellowship. E. L. and H. S. acknowledge support from the Academy of Finland. K. M. D. is supported by a National Science Foundation (NSF) Astronomy and Astrophysics Postdoctoral Fellowship under award AST-0802399. D. M. E. acknowledges support from the Spitzer Science Center from NASA grant JPL RSA-1368024. R. B. acknowledges support from NSF grant AST 05-07140. E. A. and A. B. thank the Centre National d'Etudes Spatiales and ANR-06-BLAN-0172 for support. K. L. M. acknowledges funding from the Peter and Patricia Gruber Foundation as the 2008 IAU Fellow, from the University of Portsmouth, and from the South East Physics Network. This work is based on observations and archival data obtained with the *Spitzer Space Telescope*, which is operated by the Jet Propulsion Laboratory, California Institute of Technology under a contract with NASA. Support for this work was provided by NASA. We gratefully acknowledge support from NASA JPL/Spitzer grant RSA 1374189 provided for the S^{4}G project.

REFERENCES

Abraham, R. G., Merrifield, M. R., Ellis, R. S., Tanvir, N. R., & Brinchmann, J. 1999, MNRAS, 308, 569
Athanassoula, E. 1992, MNRAS, 259, 345
———. 2003, MNRAS, 341, 1179
———. 2005, MNRAS, 358, 1477
Athanassoula, E., & Misiriotis, A. 2002, MNRAS, 330, 35
Athanassoula, E., Romero-Gómez, M., Bosma, A., & Masdemont, J. J. 2009a, MNRAS, 400, 1706
Athanassoula, E., Romero-Gómez, M., & Masdemont, J. J. 2009b, MNRAS, 394, 67
Azzollini, R., Trujillo, I., & Beckman, J. E. 2008, ApJ, 684, 1026
Bakos, J., Trujillo, I., & Pohlen, M. 2008, ApJ, 683, L103
Balcells, M., Graham, A. W., Domínguez-Palmero, L., & Peletier, R. F. 2003, ApJ, 582, L79
Barnes, D. G., et al. 2001, MNRAS, 322, 486
Bell, E. F., McIntosh, D. H., Katz, N., & Weinberg, M. D. 2003, ApJS, 149, 289
Bennert, N., Canalizo, G., Jungwiert, B., Stockton, A., Schweizer, F., Peng, C. Y., & Lacy, M. 2008, ApJ, 677, 846
Bertin, E., & Arnouts, S. 1996, A&AS, 117, 393
Bertin, G., Lin, C. C., Lowe, S. A., & Thurstans, R. P. 1989a, ApJ, 338, 78
———. 1989b, ApJ, 338, 104
Bureau, M., & Athanassoula, E. 2005, ApJ, 626, 159
Bureau, M., & Freeman, K. C. 1999, AJ, 118, 126
Buta, R., Block, D. L, & Knapen, J. H. 2003, AJ, 126, 1148
Buta, R., & Combes, F. 1996, Fundam. Cosmic Phys., 17, 95
Buta, R. J., et al. 2010, ApJ, submitted
Canalizo, G., Bennert, N., Jungwiert, B., Stockton, A., Schweizer, F., Lacy, M., & Peng, C. 2007, ApJ, 669, 801
Carey, S., Surace, J., Glaccum, W., Lowrance, P., Lacy, M., & Reach, W. 2010, IRAC Instrument Handbook (Pasadena: SSC); http://ssc.spitzer.caltech.edu/irac/iracinstrumenthandbook/
Carollo, C. M., Stiavelli, M., de Zeeuw, P. T., & Mack, J. 1997, AJ, 114, 2366
Dalcanton, J. J., et al. 2009, ApJS, 183, 67
Debattista, V. P., Carollo, C. M., Mayer, L., & Moore, B. 2004, ApJ, 604, L93
de Vaucouleurs, G., Corwin, H. G., Jr., & Bollinger, G. 1977, ApJS, 33, 229
de Vaucouleurs, G., de Vaucouleurs, A., Corwin, H. G., Jr., Buta, R. J., Paturel, G., & Fouque, P. 1991, Third Reference Catalogue of Bright Galaxies, ed. G. de Vaucouleurs, A. de Vaucouleurs, H. G. Corwin, Jr., R. J. Buta, G. Paturel, & P. Fouque (Berlin: Springer) (RC3)
Draine, B. T., & Lee, H. M. 1984, ApJ, 285, 89
Drory, N., & Fisher, D. B. 2007, ApJ, 664, 640
Durbala, A., Sulentic, J. W., Buta, R., & Verdes-Montenegro, L. 2008, preprint (arXiv:0807.2216)
Elmegreen, B. G., & Elmegreen, D. M. 1985, ApJ, 288, 438
Elmegreen, B. G., Elmegreen, D. M., & Hirst, A. C. 2004, ApJ, 612, 191
Elmegreen, B. G., Seiden, P. E., & Elmegreen, D. M. 1989, ApJ, 343, 602
Elmegreen, B. G., & Thomasson, M. 1993, A&A, 272, 37
Elmegreen, D. M., & Elmegreen, B. G. 1984, ApJS, 54, 127
Epchtein, N., et al. 1994, Ap&SS, 217, 3
Erwin, P. 2005, MNRAS, 364, 283
Erwin, P., Beltrán, J. C. V., Graham, A. W., & Beckman, J. E. 2003, ApJ, 597, 929
Erwin, P., Pohlen, M., & Beckman, J. E. 2008, AJ, 135, 20
Eskridge, P. B., et al. 2002, ApJS, 143, 73
Falcón-Barroso, J., et al. 2006, NewA Rev., 49, 515
Fazio, G. G., et al. 2004, ApJS, 154, 10
Fisher, D. B. 2006, ApJ, 642, L17
Fisher, D. B., & Drory, N. 2008, AJ, 136, 773
Friedli, D., & Benz, W. 1993, A&A, 268, 65
———. 1995, A&A, 301, 649
Gadotti, D. A. 2008, MNRAS, 384, 420
———. 2009, MNRAS, 393, 1531
———. 2010, preprint (arXiv:1003.1719)
Gil de Paz, A., et al. 2005, ApJ, 627, L29
———. 2007, ApJS, 173, 185
Giovanelli, R., et al. 2005, AJ, 130, 2598
Graham, A. W., & Worley, C. C. 2008, MNRAS, 388, 1708
Heraudeau, P., & Simien, F. 1997, A&A, 326, 897
Jarrett, T. 2004, Publ. Astron. Soc. Australia, 21, 396
Jogee, S., et al. 2004, ApJ, 615, L105
Jun, H. D., & Im, M. 2008, ApJ, 678, L97
Kang, X., van den Bosch, F. C., & Pasquali, A. 2007, MNRAS, 381, 389
Kennicutt, R. C., Jr., et al. 2003, PASP, 115, 928

Kent, S. M. 1985, ApJS, 59, 115
Kormendy, J. C., & Barentine, J. 2009, preprint (arXiv:1005.1647)
Kormendy, J., Fisher, D. B., Cornell, M. E., & Bender, R. 2009, ApJS, 182, 216
Kormendy, J., & Kennicutt, R. C., Jr. 2004, ARA&A, 42, 603
Kuijken, K., & Merrifield, M. R. 1995, ApJ, 443, L13
Laurikainen, E., & Salo, H. 2002, MNRAS, 337, 1118
Laurikainen, E., Salo, H., & Buta, R. 2005, MNRAS, 362, 1319
Laurikainen, E., Salo, H., Buta, R., & Knapen, J. H. 2007, MNRAS, 381, 401
Laurikainen, E., Salo, H., Buta, R., Knapen, J. H., & Comerón, S. 2010, MNRAS, 405, 1089
Lee, J. C., et al. 2008, in ASP Conf. Ser. 396, Formation and Evolution of Galaxy Disks, ed. J. G. Funes, & E. M. Corsini (San Francisco: ASP), 151
Martin, D. C., et al. 2005, ApJ, 619, L1
Martin, P., & Roy, J.-R 1994, ApJ, 424, 599
Méndez-Abreu, J., Aguerri, J. A. L., Corsini, E. M., & Simonneau, E. 2008, A&A, 478, 353
Menéndez-Delmestre, K., Sheth, K., Schinnerer, E., Jarrett, T. H., & Scoville, N. Z. 2007, ApJ, 657, 790
Muñoz-Mateos, J. C., Gil de Paz, A., Boissier, S., Zamorano, J., Jarrett, T., Gallego, J., & Madore, B. F. 2007, ApJ, 658, 1006
Muñoz-Mateos, J. C., et al. 2009, ApJ, 703, 1569
Naab, T., Khochfar, S., & Burkert, A. 2006, ApJ, 636, L81
Nowak, N., Thomas, J., Erwin, P., Saglia, R. P., Bender, R., & Davies, R. I. 2010, MNRAS, 403, 646
Oke, J. B. 1974, ApJS, 27, 21
Pahre, M. A., Ashby, M. L. N., Fazio, G. G., & Willner, S. P. 2004, ApJS, 154, 235
Pasquali, A., van den Bosch, F. C., & Rix, H.. 2007, ApJ, 664, 738
Paturel, G., Petit, C., Rousseau, J., & Vauglin, I. 2003a, A&A, 412, 45
Paturel, G., Petit, C., Prugniel, P., Theureau, G., Rousseau, J.Brouty, M., Dubois, P., , & Cambrésy, L. 2003b, A&A, 405, 1
Peletier, R. F., et al. 2007, NewA Rev., 51, 29
Peng, C. Y., Ho, L. C., Impey, C. D., & Rix, H. 2002, AJ, 124, 266
———. 2010, AJ, 139, 2097
Pignatelli, E., Fasano, G., & Cassata, P. 2006, A&A, 446, 373
Pohlen, M., & Trujillo, I. 2006, A&A, 454, 759
Regan, M. W., & Elmegreen, D. M. 1997, AJ, 114, 965
Regan, M. W., & Teuben, P. J. 2004, ApJ, 600, 595
Regan, M. W., et al. 2006, ApJ, 652, 1112
Rhoads, J. E. 1998, AJ, 115, 472
Romero-Gómez, M., Athanassoula, E., Masdemont, J. J., & García-Gómez, C. 2007, A&A, 472, 63
Roškar, R., Debattista, V. P., Stinson, G. S., Quinn, T. R., Kaufmann, T., & Wadsley, J. 2008, ApJ, 675, L65
Rots, A. H., Bosma, A., van der Hulst, J. M., Athanassoula, E., & Crane, P. C., 1990, AJ, 100, 387
Sakamoto, K., Okumura, S. K., Ishizuki, S., & Scoville, N. Z. 1999, ApJ, 525, 691
Salo, H., & Laurikainen, E. 2000a, MNRAS, 319, 393
———. 2000b, MNRAS, 319, 377
Sánchez-Blázquez, P., Courty, S., Gibson, B. K., & Brook, C. B. 2009, MNRAS, 398, 591
Scoville, N. Z., & Hersh, K. 1979, ApJ, 229, 578
Sheth, K., Regan, M. W., Scoville, N. Z., & Strubbe, L. E. 2003, ApJ, 592, L13
Sheth, K., Regan, M. W., Vogel, S. N., & Teuben, P. J. 2000, ApJ, 532, 221
Sheth, K., Vogel, S. N., Regan, M. W., Teuben, P. J., Harris, A. I., & Thornley, M. D. 2002, AJ, 124, 2581
Sheth, K., Vogel, S. N., Regan, M. W., Thornley, M. D., & Teuben, P. J. 2005, ApJ, 632, 217
Sheth, K., et al. 2008, ApJ, 675, 1141
Shlosman, I., Begelman, M. C., & Frank, J. 1990, Nature, 345, 679
Simard, L. 1998, in ASP Conf. Ser. 145, Astronomical Data Analysis Software and Systems VII, ed. R. Albrecht, R. N. Hook, & H. A. Bushouse (San Francisco: ASP), 108
Simkin, S. M., Su, H. J., & Schwarz, M. P. 1980, ApJ, 237, 404
Skrutskie, M. F., et al. 2006, AJ, 131, 1163
Strigari, L. E., Bullock, J. S., Kaplinghat, M., Simon, J. D., Geha, M., Willman, B., & Walker, M. G. 2008, Nature, 454, 1096
Thilker, D. A., et al. 2005, ApJ, 619, L79
———. 2007, ApJS, 173, 538
Tokunaga, A. T., Sellgren, K., Smith, R. G., Nagata, T., Sakata, A., & Nakada, Y. 1991, ApJ, 380, 452
Toomre, A. 1981, in Structure and Evolution of Normal Galaxies, ed. S. M. Fall, & D. Lynden-Bell 1980, in Proc. Adv. Study Inst., The Structure and Evolution of Normal Galaxies (Cambridge: Cambridge Univ. Press), 111
Weinzirl, T., Jogee, S., Khochfar, S., Burkert, A., & Kormendy, J. 2009, ApJ, 696, 411
Werner, M. W., et al. 2004, ApJS, 154, 1
Worthey, G. 1994, ApJS, 95, 107
Zaritsky, D., & Christlein, D. 2007, AJ, 134, 135
Zaritsky, D., & Lo, K. Y. 1986, ApJ, 303, 66
Zaritsky, D., Rix, H., & Rieke, M. 1993, Nature, 364, 313
Zaritsky, D., Zabludoff, A. I., & Gonzalez, A. H. 2008, ApJ, 682, 68